RSC Advances

PAPER

View Article Online
View Journal | View Issue

Cite this: *RSC Adv.*, 2019, **9**, 41120

Formation of toroidal Li_2O_2 in non-aqueous Li–O_2 batteries with Mo_2CT_x MXene/CNT composite†

Mihye Wu,[ab] Do Youb Kim,[bd] Hyunsoo Park,[a] Kyeong Min Cho,[a] Ju Ye Kim,[a] Seon Joon Kim,[c] Sungho Choi,[b] Yongku Kang,[bd] Jihan Kim *[a] and Hee-Tae Jung *[a]

Received 23rd September 2019
Accepted 26th November 2019

DOI: 10.1039/c9ra07699a

rsc.li/rsc-advances

Due to the growing demand for high energy density devices, Li–O_2 batteries are considered as a next generation energy storage system. The battery performance is highly dependent on the Li_2O_2 morphology, which arises from formation pathways such as the surface growth and the solution growth models. Thus, controlling the formation pathway is important in designing cathode materials. Herein for the first time, we controlled the Li_2O_2 formation pathway by using Mo_2CT_x MXene on a catalyst support. The cathode was fabricated by mixing the positively charged CNT/CTAB solution with the negatively charged Mo_2CT_x solution. After introducing Mo_2CT_x, important battery performance metrics were considerably enhanced. More importantly, the discharge product analysis showed that the functional groups on the surface of Mo_2CT_x inhibit the adsorption of O_2 on the cathode surface, resulting in the formation of toroidal Li_2O_2 *via* the solution growth model. It was supported by density functional theory (DFT) calculations that adsorption of O_2 on the Mo_2CT_x surface is implausible due to the large energy penalty for the O_2 adsorption. Therefore, the introduction of MXene with abundant functional groups to the cathode surface can provide a cathode design strategy and can be considered as a universal method in generating toroidal Li_2O_2 morphology.

Introduction

Li–O_2 batteries have been considered to be a promising candidate for high energy density energy storage systems due to their extremely high energy density (~3500 W h kg^{-1}), which is far higher than that of current Li-ion batteries.[1] The typical redox reaction mechanism of the Li–O_2 battery is the formation and decomposition of lithium peroxide (Li_2O_2); during discharge, an oxygen reduction reaction (ORR) occurs on the surface of the cathode electrode to produce Li_2O_2 as a discharge product, and during charge, electrochemical decomposition of the produced Li_2O_2 into Li^+ and O_2 occurs, that is oxygen evolution reaction (OER).[2]

Recent studies revealed that comprehension of electrochemistry and the chemistry behind the Li_2O_2 formation are crucial in determining the Li–O_2 battery performances.[4] Specifically, there are two Li_2O_2 formation models: (i) surface growth model and (ii) solution growth model.[4] In the surface growth model, since the nucleation of Li_2O_2 occurs on the surface of the cathode, the morphology of the deposited Li_2O_2 is a thin film type, resulting in small discharge capacity due to the small amount of produced Li_2O_2 but low OER overpotential due to the close contact of the thin film. In the solution growth model, since the nucleation of Li_2O_2 occurs in the solution *via* the disproportionation reaction of the soluble LiO_2 intermediate, the resultant morphology of Li_2O_2 is a toroidal structure, which leads to high discharge capacity due to the large amount of produced Li_2O_2 but a high OER overpotential due to the large particle size of toroidal Li_2O_2.[4] Thus, the formation of Li_2O_2 highly influences the electrochemical properties of the Li–O_2 batteries.

One of the most effective strategies in controlling and changing Li_2O_2 formation pathway is selecting cathode materials with different O_2 adsorbability. It is highly suggested that thin film type Li_2O_2 morphology can be obtained by using a cathode with high O_2 affinity (*e.g.* Co_3O_4 and Mo_2C) *via* the surface growth model. On the other hand, it is recommended that toroidal Li_2O_2 can be achieved by using the cathode with low O_2 affinity *via* the solution growth model.[5]

[a]*Department of Chemical and Biomolecular Engineering (BK-21 Plus), KAIST Institute for Nanocentury, Korea Advanced Institute of Science and Technology, 291 Daehak-ro, Yuseong-gu, Daejeon 34141, Republic of Korea. E-mail: Jihankim@kaist.ac.kr; heetae@kaist.ac.kr; Fax: +82-42-350-3910; +82-42-350-8452; Tel: +82-42-350-7311; +82-42-350-3931*

[b]*Advanced Materials Division, Korea Research Institute of Chemical Technology, Yuseong-gu, Daejeon 34114, Korea*

[c]*Materials Architecturing Research Center, Korea Institute of Science and Technology (KIST), Seoul 02792, Republic of Korea*

[d]*Department of Chemical Convergence Materials, Korea University of Science and Technology (UST), Yuseong-gu, Dajeon 34113, Korea*

† Electronic supplementary information (ESI) available: Details of the characterization results and calculations. See DOI: 10.1039/c9ra07699a

Here, we used MXene for the first time to control the O_2 adsorbability of the cathode, which is attributed to the surface functional groups with high coverage. MXenes are a new family of two-dimensional (2D) transition metal carbides,[6] and considered to be one of the most promising materials for energy storage systems due to their high electrical conductivity, rapid diffusion of ions and molecules, high specific surface area, and hydrophilic surfaces.[7] The general formula of MXene is $M_{n+1}X_nT_x$ ($n = 1$–3), where M stands for transition metals, X stands for nitrogen or/and carbon, and consequently, there are diverse compositions of MXenes (*e.g.* $Ti_3C_2T_x$, Ti_2CT_x, $Zr_3C_2T_x$, $Sc_4N_3T_x$, and $Nb_4C_3T_x$) with T_x representing the surface termination groups (*e.g.* oxygen, hydroxyl and fluorine), which fully cover the outer surface.[8] In general, preparing materials with high surface coverage is challenging because it is difficult to introduce surface functionality in significantly high concentrations. However, MXenes are covered by surface termination groups with extraordinarily high surface coverage,[9] which is responsible for its uniqueness. We found that MXene plays an important role in determining Li_2O_2 formation pathway in non-aqueous Li–O_2 batteries.

Experimental

Preparation of Mo_2CT_x

Mo_2CT_x was prepared by the method previously reported elsewhere.[10] Mo_2CT_x was synthesized by selective etching of gallium (Ga, Kojundo Korea, 99.99%) atoms from Mo_2Ga_2C using concentrated hydrofluoric acid (HF, Junsei, 40%). Mo_2Ga_2C was prepared by a solid–liquid reaction between Mo_2C and Ga, in a molar ratio of 1 : 8. The mixture was annealed at 850 °C for 16 hours in a vacuum furnace and cooled down to room temperature, followed by re-annealing at 850 °C for 48 hours to form Mo_2Ga_2C. Then, 2 g of Mo_2Ga_2C was placed in a polypropylene (PP) beaker with 40 ml of concentrated HF and stirred for 6 days to remove Ga atoms. The resultant powder was washed with 1 M hydrochloric acid (HCl, Daejung, 35%) and de-ionized water for several cycles until the pH of $\approx$ 7 was reached. To obtain delaminated Mo_2CT_x, 1 g of the powder was immersed in 10 ml of tetrabutylammonium hydroxide (TBAOH, Sigma-Aldrich, 57%) for 4 hours, then washed with DI water. 250 ml of DI water was added to the TBAOH-treated powder, and sonicated in an ice bath for 1 hour using a dismembrator. Then 40 ml of the above suspension was transferred to each centrifuge tube, and was centrifuged at 25 000 rpm for 5 min. The resultant supernatant was collected whereas the settled powder was removed.

Preparation of CNT/Mo_2CT_x

50 mg of carbon nanotube (CNT) was dispersed in 100 ml of DI water with cetyltrimethylammonium bromide (CTAB, Sigma-Aldrich) to produce a 0.5 mg ml^{-1} solution. 140 ml of DI water was added to 14 ml of CNT solution to produce a dilute CNT solution, and was added dropwise into the delaminated Mo_2CT_x, obtaining a weight ratio between CNT and Mo_2CT_x of 7 to 3, and it was then stirred for 1 hour. Then polystyrene bead (PS, Sigma-Aldrich, 10 wt%) was added to the above suspension to obtain the weight ratio between CNT/Mo_2CT_x to polystyrene bead as 1 to 10, and it was then sonicated for 30 min. The resultant suspension was vacuum filtrated with a membrane filter (Durapore, 0.22 μm GV), and dried at 80 °C for 12 hours. The resultant electrode was peeled off from the membrane filter, and then annealed at 450 °C for 2 hours under Ar to remove PS beads.

To clarify the effect of MXene, the CNT electrode was fabricated by the same procedure with 20 ml of CNT solution but without Mo_2CT_x.

Measurements

The surface and cross-sectional view of the CNT and CNT/Mo_2CT_x electrodes were characterized by using scanning electron microscopy (SEM, Tescan Mira 3 LMU FEG, 20 kV). The surface functional groups were identified by X-ray photoelectron spectroscopy (XPS, Thermo VG Scientific). The crystal structure of the discharged product was confirmed by X-ray powder diffractometer (XRD, Rigaku ultima IV Diffractometer) with graphite-monochromator equipped with Cu Kα line (40 kV/40 mA). The Brunauer–Emmett–Teller (BET) surface area was measured by nitrogen adsorption/desorption at 77.3 K.

The CNT and CNT/Mo_2CT_x electrodes served as the cathode, which were dried at 120 °C for 12 hours under vacuum, then assembled in an argon-filled glove box using Swagelok type cells. The average mass loading of the electrode was about 0.65 mg and the size was 12 mm in diameter.

The electrolyte was 1 M lithium nitrate ($LiNO_3$, Sigma-Aldrich) in dimethylacetamide (DMAc, Sigma-Aldrich) with water concentration <30 ppm determined by a Mettler-Toledo Karl Fischer titration. Li foil served as the anode.

Electrochemical performances were tested with a battery cycler (WBCS-3000, WonAtech) at an applied current density of 200 mA g_{CNT}^{-1} for 5 hours and 100 mA g_{CNT}^{-1} with 2.0 V cut-off, respectively, for cycle life and specific capacity measurements.

Calculations

All of the first-principle calculations were performed with the Vienna *Ab Initio* Simulation Package (VASP)[18] with the projector augmented wave (PAW)[19] potentials. In order to calculated the adsorption energy of O_2 on the surface of β-Mo_2C, the Perdue–Burke–Ernzerhof (PBE)[20] along with the dispersion force for van de Waals interactions (PBE-D3)[21] was utilized for exchange–correlation functional. The geometry optimizations were conducted with a maximum force criterion of 0.005 eV $Å^{-1}$, energy criterion of 10^{-6} eV per cell and cutoff energy of 520 eV. The initial unit-cells of β-Mo_2C and $Mo_2C(OH)_2$ were set with a vacuum space of 30 Å along the vertical direction of single layer of MXene with a Γ-centered 12 × 12 × 1 *k*-mesh. The (3 × 3) slabs were utilized for calculating the O_2 adsorption energy with a Γ-centered 4 × 4 × 1 *k*-mesh. The vibrational frequency analysis are obtained by PHONOPY[22] code. The force constants matrix was constructed by 4 × 4 × 1 supercell with density functional perturbation theory.[23]

Results and discussion

The schematic for fabricating the CNT/Mo_2CT_x cathode is described in Fig. 1. We selected carbon nanotubes (CNTs) as a catalyst support due to their excellent electrical conductivity, high mechanical strength, and facile fabrication into binder-free cathode.[11] Moreover, they provide a porous structure for better O_2 diffusion and Li_2O_2 accommodation. It is noteworthy that Mo_2CT_x was used as a catalyst simply because of its good catalytic activity in catalysis field[12] as well as easy fabrication.[10]

Since CNT was dispersed with a cationic surfactant cetyltrimethylammonium bromide (CTAB), the surface of the CNTs were positively charged; whereas the surface functional groups including –O and –OH result in the negatively charged MXene surfaces. The positively charged CNT solution was added to the negatively charged Mo_2CT_x solution to obtain uniformly attached Mo_2CT_x on the surface of CNTs in a weight ratio of 3 to 7, by the electrostatic force.[13] The PS beads were added to the mixed solution, then the resultant solution was vacuum filtered to fabricate paper type electrode. The electrode was annealed at 450 °C to create micron-sized pores in the electrode by PS removal.

SEM image shows that CNTs are well distributed over the paper type electrode with porous structure and possess well-connected networks (Fig. 2a). After introducing MXene catalyst to the CNTs, there are small Mo_2CT_x particles deposited on the CNTs (see the arrows of Fig. 2b), which were confirmed by EDS mapping in Fig. S1,† in maintaining pristine CNT morphology. Inset images of Fig. 2a and b exhibit the cross-sectional views of CNT and CNT/Mo_2CT_x electrodes, respectively, to clarify the formation of macropores after PS calcination. It has been reported that introducing pores in the paper type electrode can improve the cycle life by preventing irreversible volume expansion of the electrode, which is attributed to the growth of Li_2O_2 particles inside the paper electrode.[17] In this regard, the macropores were introduced to CNT and CNT/Mo_2CT_x electrodes to accommodate the discharge products. After PS removal, both electrodes showed highly porous structure with an average pore size of 2 μm, and the well-connected conductive networks were still maintained through the whole electrodes.

To verify the surface functionality of CNT/Mo_2CT_x electrode, X-ray photoelectron spectroscopy (XPS) measurements were conducted and the results are shown in Fig. 2c–e. The Mo 3d spectrum is composed of Mo–C, Mo^{4+}, and Mo^{6+}. The binding energy at 227.95 eV and 232 eV are assigned to the Mo–C ($3d_{5/2}$)

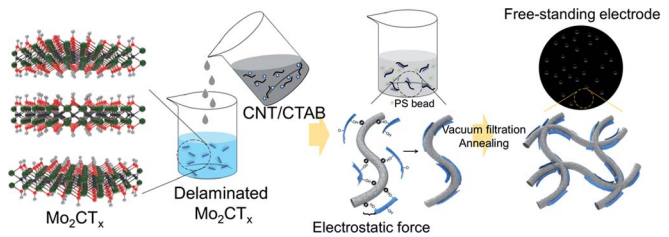

Fig. 1 Schematic of the CNT/Mo_2CT_x composite paper preparation.

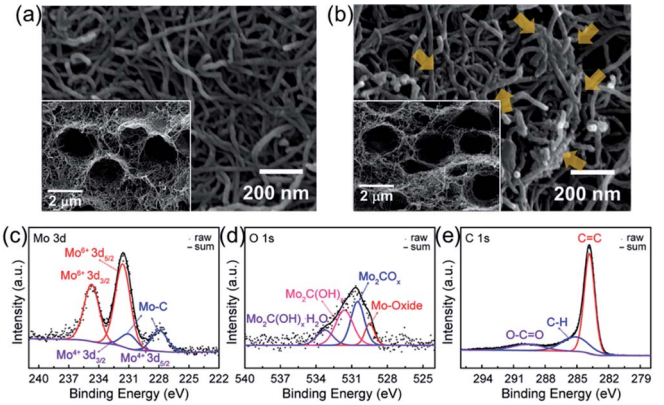

Fig. 2 SEM images of (a) CNT (top-view), (b) CNT/Mo_2CT_x (top-view) electrodes. Inset images for cross-sectional view. CNT/Mo_2CT_x (c) Mo 3d, (d) O 1s, and (e) C 1s spectra.

and Mo–C ($3d_{2/3}$) species from CNT/Mo_2CT_x.[10] The O 1s spectrum is composed of species corresponding to the Mo-oxide, Mo_2CO_x, $Mo_2C(OH)_x$, and $Mo_2C(OH)_x$–H_2O. The binding energy at 529.48 eV is assigned to the Mo-oxide, which is generated by surface oxidation.[10] The peaks at 530.5 and 531.62 eV are assigned to the –O terminated Mo_2CO_x and –OH terminated $Mo_2C(OH)_x$. The relatively small peak at 533.25 eV is assigned to $Mo_2C(OH)_x$–H_2O.[10] The C 1s spectrum is composed of components corresponding to the C=C, C–H, and O–C=O at the binding energy of 283.81, 285.13 and 289.61 eV, respectively.[14] Hence, the CNT/Mo_2CT_x electrode contains abundant functional groups including -oxide, $–O_x$, $–(OH)_x$, and $–(OH)_x$–H_2O.

To investigate the effect of the Mo_2CT_x catalyst, the electrochemical performance of the CNT/Mo_2CT_x electrode was evaluated and compared with the CNT electrode. The as-prepared paper type electrodes were assembled into the Li–O_2 cell and tested with constant current under limited capacity and limited voltage conditions. When the Li–O_2 cell was discharge with the CNT electrode at 100 mA g_{CNT}^{-1} in a 2.0 V cut-off condition, the capacity was 5950 mA h g_{CNT}^{-1} (Fig. 3a). The discharge capacity

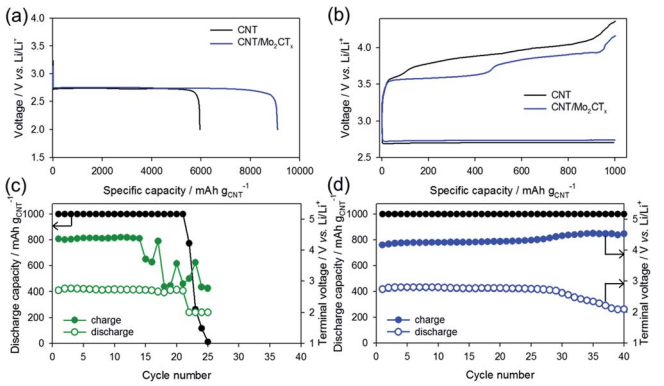

Fig. 3 (a) Discharge capacity and (b) voltage profiles of CNT and CNT/Mo_2CT_x electrodes, cycle life of (c) CNT electrode and (d) CNT/Mo_2CT_x electrode.

of the CNT/Mo_2CT_x electrode was 9100 mA h g_{CNT}^{-1}, which is much higher than that of the CNT electrode. Because the surface area of the cathode is related to the discharge capacity, it is necessary to examine the surface area of the CNT and CNT/Mo_2CT_x electrode. The BET measurements were conducted on both electrodes and the results are presented in Table S1.† Although the surface area of the CNT/Mo_2CT_x is smaller than that of the CNT, the CNT/Mo_2CT_x showed much higher discharge capacity. Thus, the Mo_2CT_x introduction greatly improves discharge capacity by promoting the Li_2O_2 formation.

On the other hand, Li–O_2 cells were cycled in a limited capacity of 1000 mA h g_{CNT}^{-1} with a current density of 200 mA g_{CNT}^{-1}. The voltage profiles of the 1st cycle were shown in Fig. 3b that the OER overpotential was reduced by the Mo_2CT_x introduction to the electrode. Moreover, the CNT/Mo_2CT_x exhibited better cycling performance over 40 cycles than that of the CNT electrode (Fig. 3c and d). In this regard, the catalytic activity of Mo_2CT_x toward Li–O_2 reactions were demonstrated and the Mo_2CT_x MXene can be considered as an effective catalyst for Li–O_2 batteries.

In order to verify the Li_2O_2 formation pathway of the Mo_2CT_x incorporated cathode, the *ex situ* XRD and SEM were carried out. The CNT/Mo_2CT_x electrode was discharged until the voltage reaches at 2.0 V with constant current of 100 mA g_{CNT}^{-1}, and then the cell was dissembled to analyse the discharge product.

The *ex situ* XRD pattern in Fig. 4a exhibited that 2 theta values at 32.89, 34.97 and 58.72 degrees correspond to the (1 0 0), (1 0 1) and (1 1 0) planes were assigned to the typical Li_2O_2 (JCPDS#01-074-0115). Thus, the discharge product was demonstrated as Li_2O_2, the main product of Li–O_2 reactions, which signifies that the prepared electrode obeys the fundamental principles of Li–O_2 batteries.

The SEM image of the discharge product (Li_2O_2) shows that the CNT/Mo_2CT_x electrode was almost covered with typical toroidal Li_2O_2 with a particle size of 1 μm (Fig. 4b). To clarify the effect of Mo_2CT_x on the toroidal Li_2O_2 formation, the CNT electrode was dissembled after discharge, then the SEM images were taken (Fig. S2†). Unlike the CNT/Mo_2CT_x electrode, the surface of the discharged CNT electrode was covered with thick deposits and sparse distribution of toroidal Li_2O_2. Thus, it is clear that this highly covered toroidal morphology is originated from the high surface coverage of MXene. The fully covered surface functional groups inhibit the access of O_2 on the surface of Mo_2C, preventing the adsorption of O_2 on Mo. Consequently, this inaccessibility of O_2 to the cathode surface hinders the nucleation of the intermediate (LiO_2) on the cathode surface, which derives the solution growth model to undergo Li_2O_2 nucleation in the electrolyte, resulting in toroidal morphology.[3] The schematic representation of the Li_2O_2 nucleation process with CNT/Mo_2CT_x electrode was illustrated in Fig. 4c.

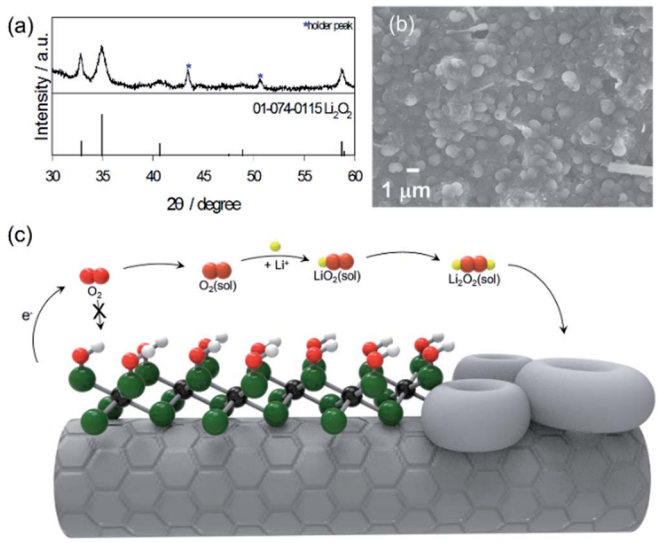

Fig. 4 (a) *Ex situ* XRD, (b) SEM image of CNT/Mo_2CT_x electrode after discharge, (c) schematic of the Li_2O_2 formation for the CNT/Mo_2CT_x electrode.

It is noteworthy that non-functionalized molybdenum carbide (Mo_2C without functional groups) has been previously reported to generate the thin film type Li_2O_2, which suggests the surface growth model for Li_2O_2 nucleation. The origin of this formation mechanism is supposed to be the lack of coordination vacancy of Mo, which leads to a strong affinity between O_2 and Mo_2C, resulting in the surface growth model of Li_2O_2. Kwak *et al.* reported the Mo_2C/carbon nanotube composite with excellent Li–O_2 battery performances, operated under 1 M $LiCF_5O_3$ in TEGDME at 100 mA g^{-1}, attributed to the formation of MoO_3-like layers on the Mo_2C nanoparticles by chemisorption of O_2 on the surface of Mo.[15] The morphology of Li_2O_2 after discharge was confirmed as a well dispersed thin layer type. Zhu *et al.* developed carbon-wrapped Mo_2C nanoparticles and CNTs on Ni foam as a cathode, operated under 1 M LiTFSI in TEGDME at 200 mA g^{-1}, and the discharge product was uniformly coated on the surface of the CNTs.[16] Since we used 1 M $LiNO_3$ in DMAc as electrolyte, which is known as a strong solution growth facilitator, it is necessary to eliminate the electrolyte effect to clarify the role of Mo_2CT_x. In this regard, the CNT/Mo_2CT_x electrode was discharged at 100 mA g^{-1} in a 2.0 V cut-off condition under 1 M LiTFSI in TEGDME, which has low donor number, and the resultant discharge product was observed by SEM. As shown in Fig. S3b,† the surface of CNT/Mo_2CT_x electrode was covered by discharge product with nearly spherical-like morphology without any thin film formation. These results imply that the Mo_2C catalyst-mediated Li_2O_2 nucleation is governed by the surface growth model.

To understand the effect of the surface functional groups on the Li_2O_2 formation pathway, density functional theory (DFT) with PBE-D3 method. The hydroxyl group (–OH) was selected as the functional group because it is the least stable species so can desorb first.[9] For the OH-terminated MXene ($Mo_2C(OH)_2$) in shown as Fig. 5a, there are three representative possible configurations (model 1: OH groups are located on the top of Mo metal; model 2: OH groups are located on the top of carbon in $Mo_2C(OH)_2$ single layer at the hollow sites; model 3: OH groups are located on the another hollow site which is position of Mo in bottom of $Mo_2C(OH)_2$ single layer). In order to calculate the O_2 adsorption on the surface of $Mo_2C(OH)_2$, the most stable model 3 of $Mo_2C(OH)_2$ was selected by the vibrational

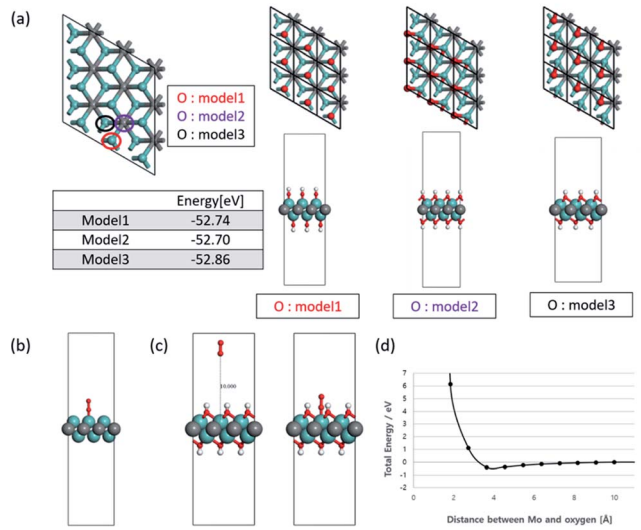

Fig. 5 (a) Representative three configurations of $Mo_2C(OH)_2$ and their total energy. The colored circles are location of oxygen atom in hydroxide. The hydrogen atom in hydroxide is omitted in the figures for convenience, (b) the optimized configuration for O_2 adsorption on $Mo_2C(OH)_2$ surface, (c) the configurations for O_2 adsorption on the surface of model 3 of $Mo_2C(OH)_2$, and (d) the fixed single-point energies in accordance with distances between the top of Mo metal from model 3 and the oxygen molecule.

frequency analysis and the energy of the geometry optimized structures when absorbing O_2. The vibrational frequency analysis indicates that $Mo_2C(OH)_2$ have some imaginary frequencies, on the other hand, Mo_2C have a no imaginary frequency in Fig. S4.† These tendencies are also found in α-Mo_2C[24] as well as β-Mo_2C. Although $Mo_2C(OH)_2$ have dynamic instability from the analysis of phonon dispersion, model 3 is regarded as at least the most stable structure because model 3 have the lowest geometry optimized energy (−52.86 eV) and only one small imaginary frequency when comparing model 1 and 2 (each −52.74 and 52.70 eV).

As such, the OH-terminated MXene for model 3 was selected as the configuration to examine the binding energy of O_2. The 3 × 3 slabs of Mo_2C and $Mo_2C(OH)_2$ were utilized for the adsorption energy of O_2. At first, non-terminated Mo_2C surface was computed to be −272 kJ mol^{-1} (Fig. 5b), while that of $Mo_2C(OH)_2$ led to non-convergent result. As such, the position of all the atoms were fixed in the simulations to obtain the fixed single-point energies for varying O_2 positions relative to the $Mo_2C(OH)_2$ surface (Fig. 5c). Specifically the O_2 molecule was initialized at a distance 10 Å from top of the Mo metal with subsequent configurations coming closer to the top of the Mo metal from model 3. The resulting single point energy data (Fig. 5d) reveals that O_2 cannot bind to the surface of $Mo_2C(OH)_2$, implying that LiO_2 nucleation as well as Li_2O_2 cannot possibly occur on the surface of Mo_2CT_x surface. This is consistent with the experimental finding and corroborates that the toroidal Li_2O_2 formation pathway is resulted from the inaccessibility of O_2 on the cathode surface.

Conclusions

We found that MXene with abundant functional groups not only enhanced the battery performance but also played a significant role in determining the Li_2O_2 formation pathway. The discharge capacity, overpotential and cycle life were improved by introducing Mo_2CT_x on CNTs, which manifest that the Mo_2CT_x exhibits good catalytic activity toward Li–O_2 reactions. The high surface coverage of Mo_2CT_x with functional groups resulted in the toroidal Li_2O_2 formation *via* the solution growth model. This is attributed to the inaccessibility of O_2 to the cathode surface, which was verified by the DFT calculations.

It is noticeable that here we only studied one type of MXene, but more diverse MXenes can play a critical role in determining the Li_2O_2 formation pathway due to their extraordinarily high surface coverage. We believe this study will provide guidelines for a large family of MXenes to be considered as effective catalysts for the Li–O_2 batteries in the future.

Conflicts of interest

There are no conflicts to declare.

Acknowledgements

This research was supported by the Korea Research Institute of Chemical Technology (project No. KK1922-20) and the National Research Foundation of Korea (NRF) funded by the Ministry of Education, Science and Technology (MEST) (NRF-2015K1A4A3047100) and the National Research Foundation of Korea (NRF) grant funded by the Ministry of Science and ICT (MSIT) (2018R1A2B3008658) and Future Planning, Korea. This research was also supported in part by Energy Cloud R&D Program (NRF-2019M3F2A1072233) through NRF (National Research Foundation of Korea) funded by Ministry of Science and ICT.

References

1 P. G. Bruce, S. A. Freunberger, L. J. Hardwick and J.-M. Tarascon, *Nat. Mater.*, 2012, **11**, 19.
2 F. Li, T. Zhang and H. Zhou, *Energy Environ. Sci.*, 2013, **6**, 1125; W. Zhou, H. Zhang, H. Nie, Y. Ma, Y. Zhnag and H. Zhang, *ACS Appl. Mater. Interfaces*, 2015, **7**, 3389.
3 Z. Lyu, Y. Zhou, W. Dai, X. Cui, M. Lai, L. Wang, F. Huo, W. Huang, Z. Hu and W. Chen, *Chem. Soc. Rev.*, 2017, **46**, 6046.
4 D. Aurbach, B. D. McCloskey, L. F. Nazar and P. G. Bruce, *Nat. Energy*, 2016, **1**, 16128; L. Johnson, C. Li, Z. Liu, Y. Chen, S. A. Freunberger, P. C. Ashok, B. B. Praveen, K. Dholakia, J.-M. Tarascon and P. G. Bruce, *Nat. Chem.*, 2014, **6**, 1091; N. B. Aetukuri, B. D. McCloskey, J. M. Garcia, L. E. Krupp, V. Viswanathan and A. C. Luntz, *Nat. Chem.*, 2015, **7**, 50.
5 Z. Lyu, L. Yang, Y. Luan, X. R. Wang, L. Wang, Z. Hu, J. Lu, S. Xiao, F. Zhang, X. Wang, F. Huo, W. Huang, Z. Hu and W. Chen, *Nano Energy*, 2017, **36**, 68.

6 S. J. Kim, H.-J. Koh, C. E. Ren, O. Kwon, K. Maleski, S.-Y. Cho, B. Anasori, C.-K. Kim, Y.-K. Choi, J. Kim, Y. Gogotsi and H.-T. Jung, *ACS Nano*, 2018, **12**, 986; S. J. Kim, M. Naguib, M. Zhao, C. Zhang, H.-T. Jung, M. W. Barsoum and Y. Gogotsi, *Electrochim. Acta*, 2015, **163**, 246; M. Naguib, M. Kurtoglu, V. Presser, J. Lu, J. J. Niu, M. Heon, L. Hultman, Y. Gogotsi and M. W. Barsoum, *Adv. Mater.*, 2011, **23**, 4248.

7 M. Naguib, O. Mashtalir, J. Carle, V. Presser, J. Lu, L. Hultman, Y. Gogotsi and M. W. Barsoum, *ACS Nano*, 2012, **6**, 1322; M. R. Lukatskaya, O. Mashtalir, C. E. Ren, Y. Dall'Agnese, P. Rozier, P. L. Taberna, M. Naguib, P. Simon, M. W. Barsoum and Y. Gogotsi, *Science*, 2013, **341**, 1502; M. Ghidiu, S. Kota, J. Halim, A. W. Sherwood, N. Nedfors, J. Rosen, V. N. Mochalin and M. W. Barsoum, *Chem. Mater.*, 2017, **29**, 1099; Q. Tang, Z. Zhou and P. Shen, *J. Am. Chem. Soc.*, 2012, **134**, 16909.

8 B. Anasori, M. R. Lukatskaya and Y. Gogotsi, *Nat. Rev. Mater.*, 2017, **2**, 16098.

9 J. L. Hart, K. Hantanasirisakul, A. C. Lang, B. Anasori, D. Pinto, Y. Pivak, J. T. van Omme, S. J. May, Y. Gogotsi and M. L. Taheri, *Nat. Commun.*, 2019, **10**, 522.

10 J. Halim, S. Kota, M. R. Lukatskaya, M. Naguib, M.-Q. Zhao, E. J. Moon, J. Pitock, J. Nanda, S. J. May, Y. Gogotsi and M. W. Barsoum, *Adv. Funct. Mater.*, 2016, **26**, 3118.

11 Y. Li, Y. Huang, Z. Zhang, D. Duan, X. Hao and S. Liu, *Chem. Eng. J.*, 2016, **283**, 911.

12 Z. W. Seh, K. D. Fredrickson, B. Anasori, J. Kibsgaard, A. L. Strickler, M. R. Lukatskaya, Y. Gogotsi, T. F. Jaramillo and A. Vojvodic, *ACS Energy Lett.*, 2016, **1**, 589.

13 X. Xie, M.-Q. Zhao, B. Anasori, K. Maleski, C. E. Ren, J. Li, B. W. Byles, E. Pomerantseva, G. Wang and Y. Gogotsi, *Nano Energy*, 2016, **26**, 513.

14 A. Byeon, C. B. Hatter, J. H. Park, C. W. Ahn, Y. Gogotsi and J. W. Lee, *Electrochim. Acta*, 2017, **258**, 979.

15 W.-J. Kwak, K. C. Lau, C.-D. Shin, K. Amine, L. A. Curtiss and Y.-K. Sun, *ACS Nano*, 2015, **9**, 4129.

16 Q.-C. Zhu, S.-M. Xu, M. M. Harris, C. Ma, Y.-S. Liu, X. Wei, H.-S. Xu, Y.-X. Zhou, Y.-C. Cao, K.-X. Wang and J.-S. Chen, *Adv. Funct. Mater.*, 2016, **26**, 8514.

17 D. Y. Kim, M. Kim, D. W. Kim, J. Suk, O. O. Park and Y. Kang, *Carbon*, 2015, **93**, 625.

18 G. Kresse and J. Hafner, *Phys. Rev. B: Condens. Matter Mater. Phys.*, 1993, **48**, 17; G. Kresse, J. Furthmüller and J. Hafner, *Phys. Rev. B: Condens. Matter Mater. Phys.*, 1994, **50**, 58; G. Kresse, *Phys. Rev. B: Condens. Matter Mater. Phys.*, 1996, **54**, 16.

19 P. E. Blöchl, *Phys. Rev. B: Condens. Matter Mater. Phys.*, 1994, **50**, 24.

20 J. P. Perdew, K. Burke and M. Ernzerhof, *Phys. Rev. B: Condens. Matter Mater. Phys.*, 1996, **77**, 18.

21 S. Grimme, S. Ehrlich and L. Goerigk, *J. Comput. Chem.*, 2011, **32**, 1456.

22 A. Togo, F. Oba and I. Tanaka, *Phys. Rev. B: Condens. Matter Mater. Phys.*, 2008, **78**, 134106.

23 S. Baroni, S. de Gironcoli and A. D. Corso, *Rev. Mod. Phys.*, 2001, **73**, 2.

24 J. Lei, A. Kutana and B. I. Yakobson, *J. Mater. Chem. A*, 2017, **5**, 3438.